Formation of Extreme Cold-Air Pools in Elevated Sinkholes: An Idealized Numerical Process Study

GÜNTHER ZÄNGL

Meteorologisches Institut der Universität München, Munich, Germany

(Manuscript received 16 June 2004, in final form 15 September 2004)

ABSTRACT

High-resolution numerical simulations with the fifth-generation Pennsylvania State University–National Center for Atmospheric Research (PSU–NCAR) Mesoscale Model (MM5) are presented to investigate the processes leading to the formation of extreme cold-air pools in elevated sinkholes. The simulations are idealized in the sense that they are conducted with idealized model topography and with idealized large-scale conditions representing an undisturbed wintertime high pressure situation. After a number of model modifications, the temperature fields, radiative cooling rates, and sensible heat fluxes simulated by the model were in good agreement with the available observations, giving confidence that the model is suitable for this process study.

The model results indicate a number of necessary preconditions for the formation of an extreme cold-air pool in a sinkhole. Apart from undisturbed clear weather, a small heat conductivity of the ground and an effective mechanism drying the low-level air during the cooling process are required. The importance of the heat conductivity results from the fact that the net cooling of the ground is only a small residual between the net radiative heat loss and the ground heat flux. As a consequence, extreme cooling events are strongly favored by the presence of freshly fallen powder snow. The necessity of a drying mechanism is related to the strong temperature dependence of the saturation vapor pressure, decreasing by a factor of about 2.5 per 10 K temperature decrease at temperatures below −20°C. Except in cases of very dry ambient air, a nocturnal cooling by 25 or 30 K (as observed in extreme cases) must be accompanied by an order-of-magnitude reduction of the water vapor mixing ratio to prevent the formation of fog. According to the simulations, the most effective drying mechanism is provided by the formation of ice clouds and the subsequent sedimentation of the ice particles. Near the surface, direct deposition of water vapor at the ground also seems to play a significant role.

1. Introduction

About 75 yr ago, the first temperature measurements in the Gstettneralm sinkhole (Austria) revealed the frequent occurrence of extremely low temperature minima at the bottom of the sinkhole (Schmidt 1930). During the measurement period from 1928 to 1942, minima below −50°C were recorded several times, and minima below −35°C turned out to be quite a common feature in clear winter nights (Aigner 1952). The temperature differences between the bottom of the sinkhole and locations along the side slopes above the lowest outflow were found to range between 25 and 30 K in the presence of freshly fallen snow and between 10 and 15 K in the absence of snow cover (Sauberer and Dirmhirn 1954, 1956). From autumn 2001 through summer 2002, another measurement campaign was conducted in the Gstettneralm sinkhole in order to get a better insight into the mechanisms of cold-pool formation and breakup and to get more precise measurements of the energy and mass budgets (Pospichal et al. 2003, Whiteman et al. 2004a,b). Another sinkhole that has been the subject of a recent measurement campaign is the Peter Sinks basin in Utah (Clements et al. 2003).

The presently available data reveal that during undisturbed clear nights, the air in closed sinkholes cools very rapidly around sunset, followed by a more gradual cooling in the night proper. The cooling rate of the basin air is found to be close to the net radiative cooling rate around sunset but much smaller in the second half of the night, implying that a significant opposing heat source is present. Clements et al. (2003) also found that downslope flows along the side slopes of the basin are only of minor importance because they are hampered by the extreme static stability within the cold pool. Moreover, turbulent vertical fluxes of sensible heat were shown to be negligible except for a short period after sunset, indicating that the cooling of the basin air is maintained by radiative heat flux divergence. The absence of significant sensible heat fluxes also suggests that the net radiative heat loss of the surface is nearly

Corresponding author address: Günther Zängl, Meteorologisches Institut der Universität München, Theresienstraße 37, D-80333 Munich, Germany.
Email: guenther@meteo.physik.uni-muenchen.de

balanced by heat conduction from the ground, but measurements of the latter quantity have not been conducted so far.

Previous theoretical and numerical modeling work dealing with cold-air pools mainly focused on processes destroying the cold pool. Whiteman and McKee (1982) developed a semianalytical model describing the evolution of inversion breakup given a certain heat input. Numerical simulations of inversion breakup induced by radiative heating were conducted, for example, by Bader and McKee (1983) and more recently by Colette et al. (2003), the latter authors emphasizing the impact of topographic shading. Among the dynamical processes capable of removing cold-air pools, turbulent vertical mixing has received the largest attention (Petkovšek 1985, 1992; Rakovec et al. 2002; Zhong et al. 2003). The adjustment of the cold air mass to a horizontal pressure gradient imposed at the top of the cold pool was investigated by Petkovšek and Vrhovec (1994) and Zängl (2003a). Zängl (2003a) also considered the impact of cold-air drainage and the side effects of upstream blocking on turbulent vertical mixing. Comparatively few studies consider the formation of cold-air pools due to radiative cooling or advective warming at higher levels (Vrhovec 1991; Zhong et al. 2001), and there seems to be no published modeling work so far that considers such extreme situations as in the Gstettneralm or Peter Sinks sinkholes.

Accordingly, the goal of the present study is to undertake a first attempt to simulate the formation and evolution of extreme cold-air pools with a widely used mesoscale numerical model. Besides demonstrating the ability of the model to realistically reproduce the observed characteristics of such extreme cold pools (which required several adaptations of the model code), we would like to investigate the surface heat balance in the center region of the sinkhole. In particular, evidence will be presented that the net radiative heat loss is indeed to a large extent balanced by the ground heat flux. Moreover, the drying of the basin air accompanying the cooling process, which has received very little attention so far, will be examined in detail. The importance of the drying processes lies in the fact that for typical atmospheric humidities, a temperature difference of order 25 K between the sinkhole bottom and the ambient air implies that the absolute humidity (or the mixing ratio) within the sinkhole is several times smaller than in the ambient air. Otherwise, the formation of fog would have prevented the development of such a large temperature difference.

The outline of the paper is as follows. After describing the model and the setup of the simulations in section 2, the evolution of the simulated cold-air pool is described and discussed in section 3. Section 4 is dedicated to studying the surface heat balance and the drying processes. A summary of the most important results is provided in section 5.

2. Model and setup

The numerical simulations presented in this study have been conducted with the fifth-generation Pennsylvania State University–National Center for Atmospheric Research Mesoscale Model (MM5, version 3.3) (Grell et al. 1995). The model solves the nonhydrostatic equations of motion in a terrain-following sigma coordinate system. Five interactively nested model domains are used, the horizontal mesh sizes being 20.25 km, 6.75 km, 2.25 km, 750 m, and 250 m, respectively. The corresponding numbers of grid points are 79×79 for the first three domains, 73×73 for the fourth domain, and 61×79 for the fifth domain. In the vertical, 51 full-sigma levels are used, corresponding to 50 half-sigma levels where all variables but the vertical wind are computed. The lowermost half-sigma level is located about 7.5 m above ground, and the vertical distance between the model layers is about 15 m in the lowermost 120 m. Higher above, the distance between the model layers gradually increases, reaching about 700 m near the upper boundary, which is located at 100 hPa. Model output data taken from the lowermost half-sigma level is referred to as surface fields throughout the paper.

An idealized topography is used for our present simulations, representing a mountain range with four peaks and an embedded sinkhole (see Fig. 1). It is given by

$$h(x, y) = h_0 \frac{[1 - 0.1 \cos(\pi x/l_x)]\,[1 - 0.1 \cos(\pi y/l_y)]}{(1 + |x/L_x|^{\alpha})^{1.5}(1 + |y/L_y|^{\beta})^{1.5}}, \tag{1}$$

with $h_0 = 1500$ m, $l_x = 7.5$ km, $l_y = 5$ km, $L_x = 10$ km, $L_y = 15$ km, $\alpha = 4$, and $\beta = 5$. The horizontal dimensions of this model sinkhole are 3–5 times larger than those of the real sinkholes mentioned above (Gstettneralm and Peter Sinks), which was necessary to ensure a proper resolution of the sinkhole while keeping the computing time requirements within reasonable bounds. The height difference between the bottom of the sinkhole and the lowest outflow is about 100 m, which is twice as much as for the Gstettneralm sinkhole and 3 times as much as for Peter Sinks. Consequently, the depth-to-width ratio of the model sinkhole is reasonably realistic, and the layer spacing of 15 m implies that seven model layers are available for resolving the central part of the expected cold pool. The surface is assumed to be covered with freshly fallen snow above a height of 1000 m, which affects the whole basin and the surrounding mountains. At lower heights, a grass-covered surface is assumed. These choices correspond to a surface albedo of 0.7 and 0.25, respectively, and the heat capacity of the ground is set to 3×10^5 J K^{-1} m^{-3} for snow and to 1.5×10^6 J K^{-1} m^{-3} for grass. A sensitivity experiment with grassland everywhere is also conducted (see Table 1 for a summary of the sensitivity tests).

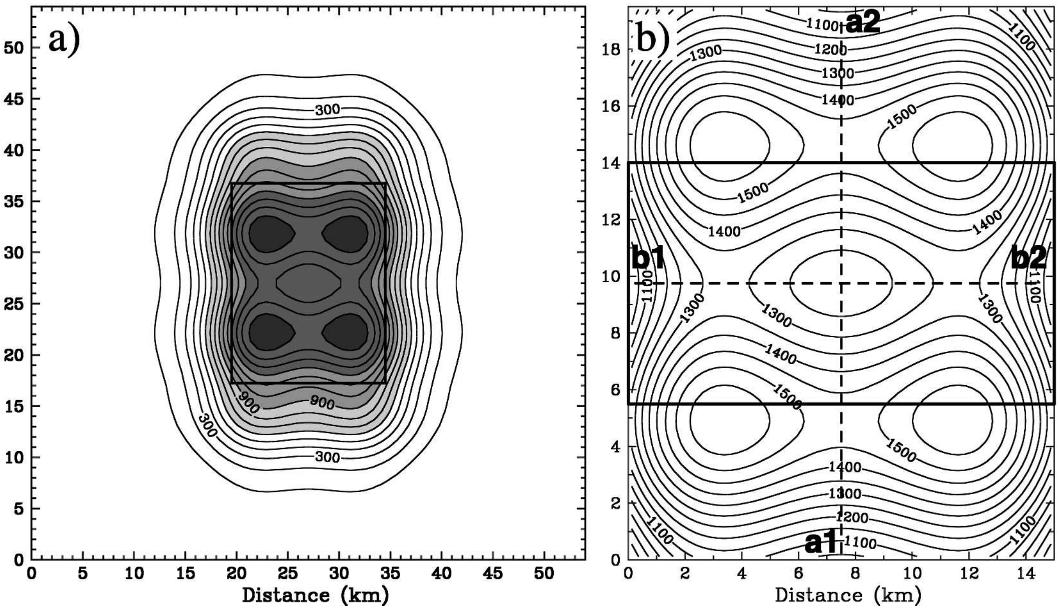

FIG. 1. Topography of the simulations. (a) Fourth model domain (mesh size 750 m); contour interval 100 m, and shading starts at a height of 600 m with increments of 300 m. The rectangle indicates the location of the fifth domain [(b)]. (b) Fifth model domain (mesh size 250 m); contour interval 50 m. The rectangle indicates the subdomain shown in Figs. 2, 3, 6, 10, 11, and 12, and the dashed lines indicate the position of the vertical cross sections a1–a2 and b1–b2.

The initial and boundary conditions used for running the model are highly idealized as well but are chosen to lie within the observed range of variability. To investigate the evolution of the cold-air pool under undisturbed conditions, the absence of large-scale winds and horizontal pressure gradients is assumed. The initial temperature profile starts with a sea level temperature of 272.5 K, followed by a vertical temperature gradient of -6.5 K km^{-1} up to the tropopause, which is specified to be at 225 hPa. Higher above, an isothermal stratosphere is assumed. The initial relative humidity is set to 50% in the troposphere and to 10% in the stratosphere, implying that the formation of clouds is possible only as a result of substantial radiative cooling. Sensitivity experiments are conducted with a halved tropospheric humidity and with a 10-K-colder sea level temperature (see again Table 1). In the latter test, the vertical temperature gradient and the initial relative humidity are the same as in the reference case, implying that the water vapor mixing ratio is reduced by a factor between 2 and 3. The integrations are performed with a constant Coriolis parameter of 10^{-4} s^{-1}, and a latitude of 50°N is assumed for computing radiation. The model date, which also enters into the computation of radiation, is set to 15 December. All simulations are started at a local time of 12 h and are conducted for 24 h. During the integrations, the temperature profile imposed at the lateral model boundaries varies with time in the boundary layer such as to be consistent with the radiative heating/cooling present in the flat part of the model domain.

To allow for a meaningful analysis of the physical processes involved in the formation of cold-air pools, a sophisticated set of physics parameterizations is used. Cloud microphysics are treated with the so-called Reisner2 scheme that has prognostic equations for cloud water, cloud ice, cloud ice particle number concentration, rain, snow and graupel (Reisner et al. 1998). Although the large-scale conditions chosen for the simulations do not favor the generation of precipitation, the formation and sedimentation of cloud ice will prove to be of crucial importance for the drying process within the cold-air pool. A sensitivity experiment is conducted with the simpler Reisner1 scheme that does not have separate variables for graupel and the ice number concentration. The radiation scheme accounts for interactions with moisture and clouds (Grell et al. 1995; Mlawer et al. 1997) and is called every 6 min. Following the formulas given by Garnier and Ohmura (1968), it was modified by the author so as to include the effects of sloping topography and topographic shading on the

TABLE 1. List of simulations. See section 2 for further details.

Simulation	Description
REF	Reference simulation
COLD	10-K-colder initial temperature profile
DRY	Halved initial relative humidity
GRASS	Surface parameters for grassland instead of snow
R1	Reisner1 cloud microphysics
PBL	Original thresholds for TKE and friction velocity in the PBL scheme

flux of direct solar radiation. However, three-dimensional effects on longwave radiative transfer are not accounted for. This is acceptable for gently sloping sinkholes like Peter Sinks or Gstettneralm (and the idealized one considered here), but it would not be appropriate for steeper sinkholes having a sky-view factor well below 1 (Whiteman et al. 2004b). The planetary boundary layer is parameterized using the Gayno–Seaman scheme (Shafran et al. 2000), which integrates a prognostic equation for turbulent kinetic energy (TKE) and parameterizes vertical mixing as a function of the local TKE value. This scheme also had to be modified in several aspects to become suitable for this study. The first change was to remove a sign check that effectively prevents the condensation or deposition of water vapor at the surface. In addition, the calculation of the saturation water vapor pressure at the surface, which enters into the computation of the surface moisture flux, has been changed such as to use the saturation pressure over ice (rather than supercooled water) below the freezing point. Moreover, the (arbitrary) lower threshold values applied to the vertical diffusion coefficient (0.5 $m^2 s^{-1}$ near the surface) were commented out, and the lower thresholds for the TKE ($10^{-3} m^2 s^{-2}$) and the friction velocity (0.1 m s^{-1}) were relaxed to $10^{-7} m^2 s^{-2}$ and 0.005 m s^{-1}, respectively. As will be demonstrated in another sensitivity test, retaining the original thresholds for the TKE and the friction velocity already leads to unrealistic heat fluxes within the cold pool. Another important modification affects the implementation of the horizontal numerical diffusion, which is computed along the terrain-following sigma surfaces in the original MM5. Since this induces large systematic errors for variables having a strong vertical stratification, the diffusion is computed truly horizontally for the temperature, the water vapor mixing ratio, and the cloud variables in the modified version (Zängl 2002). As demonstrated by Zängl (2003a), using this modified diffusion scheme is of crucial importance for a meaningful simulation of the evolution of cold-air pools. Finally, the generalized vertical coordinate described by Zängl (2003b) is used. It allows for a rapid decay with height of the topographic structures in the coordinate surfaces, further reducing the occurrence of numerical errors in high-resolution simulations over steep terrain.

3. Results

a. Reference run

We start our discussion of the results with a look at the simulated evolution of the temperature and moisture field of the reference (REF) run. Surface fields (taken from the lowermost model level) of wind speed, water vapor mixing ratio, and temperature are displayed in Figs. 2 and 3 for 1600 local time (LT) and 0800 LT, respectively. These times correspond to the first and last full hours of the astronomical night. Figures 2 and 3 also show the ground temperature fields for the respective times, defined as the temperature representative for the uppermost centimeter of the soil (or snow). Vertical cross sections of potential temperature, wind speed, and cloud water/ice are shown in Fig. 4, and selected time series for the sinkhole center are provided in Fig. 5.

The 1600 LT fields displayed in Fig. 2 represent the situation about 35 min after sunset. The surface wind field (Fig. 2a) shows almost calm conditions in the interior of the sinkhole, while significant (~2 m s^{-1}) downslope winds are evident at the northern and southern side slopes. These katabatic downslope winds are asymmetric, which is mainly related to the fact that the solar radiation computed during daytime accounts for the slope orientation and topographic shadowing. Moreover, they are restricted to the upper part of the side slopes, lying above the saddle points on the western and eastern sides of the sinkhole (see also Figs. 4a and 4c). In the closed part of the sinkhole, the stratification is already too stable for significant downslope winds to occur. Even stronger (up to 6 m s^{-1}) katabatic winds are found to the west and to the east of the sinkhole, representing an outflow of cold air that has accumulated in the basin.

The water vapor mixing ratio at the lowermost model level (Fig. 2b) exhibits a minimum in the center of the basin, surrounded by a ring of moister air. Outside the basin area, the air is drier again. A comparison with the mixing ratio field 1 h earlier (not shown) reveals that this structure is mainly related to two different drying processes. While the subsidence related to the katabatic winds dries the air outside the basin, the reduction of the water vapor mixing ratio in the sinkhole center is mainly related to condensation (conversion into cloud water; see also Fig. 4e). The ring of moister air in between reflects an area that has experienced only a weak drying during the preceding hour.

Figures 2c and 2d show the starting phase of the cold-air-pool formation in the sinkhole. The temperature difference between the sinkhole center and outside is about 8 K. Moreover, there is quite a large difference between the ground temperature and the air temperature at 7.5 m AGL (up to 9 K). As is discussed in section 4, this is related to the fact that the dominant cooling process in the preceding hour is net radiative heat loss from the ground. However, the cloud formation already mentioned abruptly diminishes the temperature difference between the ground and the near-surface air after 1600 LT.

During the night, the cooling and drying of the air in the basin proceeds. The model results at 0800 LT show that the surface wind field is structurally similar to that obtained for 1600 LT on the preceding day, but the cold-air outflow from the basin has further intensified (up to 8 m s^{-1}; Fig. 3a). On the other hand, the air in the interior of the basin is even calmer than at 1600 LT. The

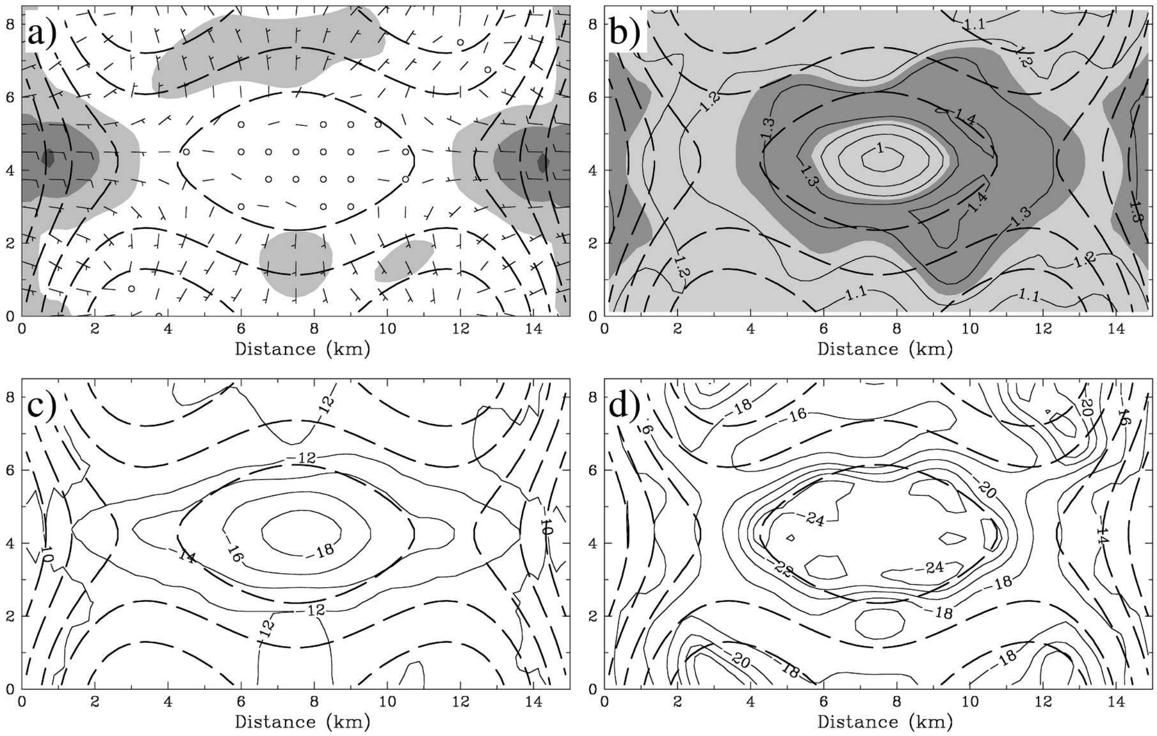

FIG. 2. Results of the REF run at 1600 LT for the subdomain indicated in Fig. 1b. Bold dashed lines indicate the topography with a contour interval of 100 m. (a) Surface wind field; full barb = 5 m s^{-1}. Shading denotes the absolute wind speed with an increment of 2 m s^{-1}, and circles indicate a wind speed of less than 0.25 m s^{-1}. (b) Surface water vapor mixing ratio; contour interval 0.1 g kg^{-1}, and shading starts at 0.75 g kg^{-1} with increments every 0.5 g kg^{-1}. (c) Surface air temperature; contour interval 2°C. (d) Ground temperature; contour interval 2°C.

mixing ratio in the basin center has decreased by more than 50% (Fig. 3b), which also allowed for a further decrease of the air temperature by about 10 K (Fig. 3c). As is shown in section 4, the drying is mainly achieved by ice cloud formation and subsequent sedimentation of the ice particles. The air in the center region of the sinkhole is now more than 15 K colder than outside, which in turn explains the virtual absence of katabatic winds in the inner part of the sinkhole. A comparison between Figs. 3c and 3d also reveals that the difference between ground and air temperature is only about 1 K in the center region, while it is still above 5 K over parts of the northern and southern slopes. This interesting structure of the ground–air temperature difference is closely related to the presence of clouds in the center region of the basin (see Fig. 4f). The clouds increase the downward longwave radiation reaching the ground, thereby reducing the net radiative cooling of the ground, and on the other hand, they increase the direct radiative cooling of the air. Both effects act to keep the ground–air temperature difference small. The larger ground–air temperature differences occur in the cloud-free regions where the net radiative heat loss of the ground is much larger (see also Fig. 10a).

Vertical cross sections along the lines a1–a2 and b1–b2 indicated in Fig. 1b are displayed in Fig. 4. The south–north cross sections (a1–a2) in Figs. 4a and 4b confirm that significant katabatic winds are restricted to the upper part of the basin where the static stability is comparatively weak. Moreover, it is evident that the depth of the cold pool increases substantially during the night. Near the side slopes, the isentropes are seen to bend upward, reflecting the radiative cooling of the surface. The west–east cross sections in Figs. 4c and 4d show the structure of the lateral cold-air outflow already mentioned above. The depth and strength of this cold-air outflow increases during the night along with the deepening of the cold-air pool. Finally, the distribution of cloud water and cloud ice is shown in Figs. 4e and 4f. At 1600 LT, a water cloud with mixing ratios up to 0.17 g kg^{-1} is found at the bottom of the sinkhole, leading to a rapid increase of the ground temperature in the subsequent hour. By 0800 LT on the following day, the depth of the fog cloud has substantially increased, but the mixing ratios in the center region of the basin are much smaller than in the early evening. The depletion of the cloud water is due to the presence of cloud ice (solid lines in Fig. 4f), which grows at the expense of the cloud water because the vapor pressure is lower over ice than over water. Since cloud ice has a significant sedimentation speed (which is accounted for in the Reisner microphysics schemes of the MM5), the cloud

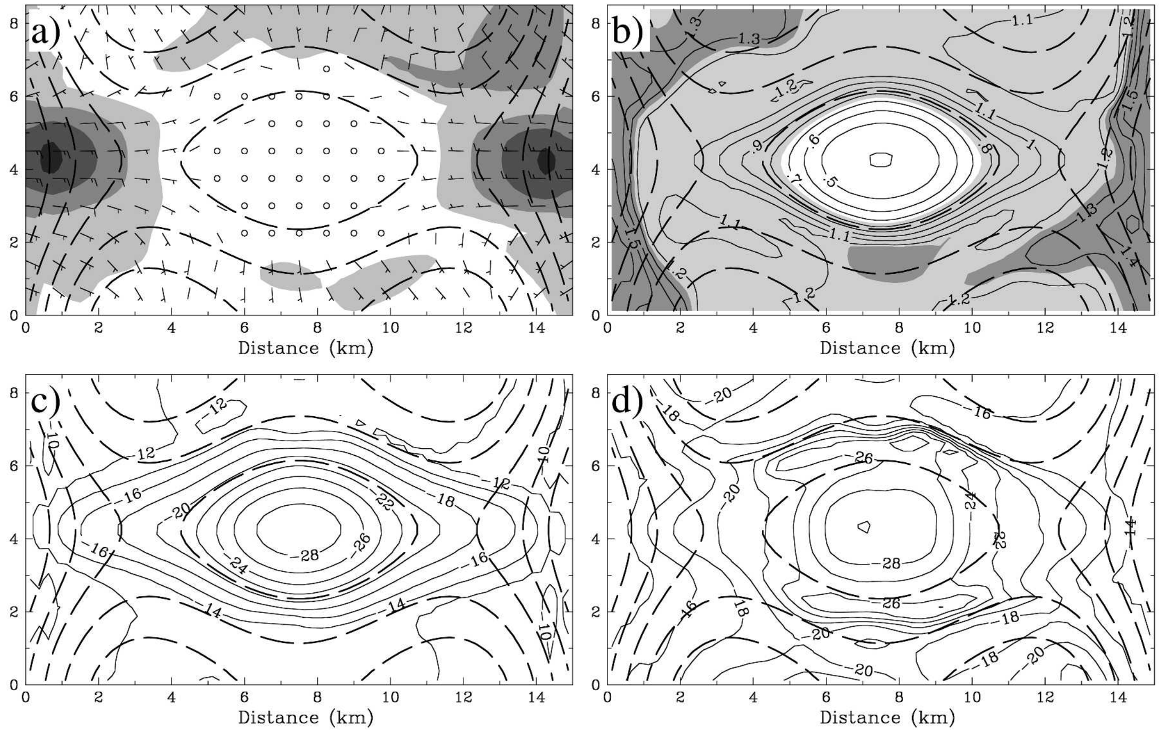

FIG. 3. Same as Fig. 2, but for 0800 LT.

ice then falls to the ground and leaves behind "freeze-dried" air. Part of the cloud ice also gets converted into snow in the model (not shown), which further accelerates the drying process because snow has a larger fall speed than cloud ice. Larger cloud water mixing ratios (up to 0.14 g kg^{-1}) are still present along the side slopes at an altitude of about 1.3 km where the higher temperature leads to smaller amounts of cloud ice and thus to a less effective depletion process. The cloud formation along the side slopes of the basin is probably also affected by the horizontal numerical diffusion applied in the MM5. Although this diffusion is applied in a truly horizontal manner in the modified model code (Zängl 2002), which is much more accurate than computing the diffusion along the terrain-following coordinate surfaces, there is still a feature that might not be fully realistic: The truly horizontal diffusion tends to induce a moisture transport from the interior of the basin toward the side slopes because at a given height, the water vapor mixing ratio decreases toward the side slopes. This in turn is because the saturation mixing ratio of the radiatively cooled air above the slope is smaller than the actual mixing ratio in the interior of the basin (at the same height), so that condensation maintains this horizontal mixing ratio gradient. Unfortunately, a significant reduction of the diffusion coefficient is not feasible because this tends to induce numerical noise.

To complete the description of the REF run, Fig. 5 shows time series of surface temperature, ground temperature, and surface water vapor mixing ratio for the center point of the sinkhole. Starting at −8°C, the near-surface air has already cooled by 5 K during the first 3 h of simulation because the high surface albedo of 70% renders the net radiative heat flux negative even around noon. The strong radiative heat loss, which is discussed in more detail in section 4, becomes also manifest in a large temperature difference between the near-surface air and the ground. After clouds have formed, the ground becomes warmer than the near-surface air for about 2 h. Later on, the temperature difference becomes negative again but hardly exceeds 1 K for the rest of the night. The total cooling between model startup and next day's sunrise amounts to slightly more than 20 K for both the ground and the near-surface air. Figure 5c shows that the near-surface air in the sinkhole center dries by a factor of more than 3 during the simulation, the drying rate being largest in the early evening and becoming small after midnight. The other results displayed in Fig. 5 are discussed in the next subsection.

b. Sensitivity experiments

A number of sensitivity experiments have been carried out to test the influence of the initial humidity and temperature, the surface parameters assumed in the sinkhole region, and the physics parameterizations used in the model. Five of them will be discussed in the following. They are named COLD, DRY, GRASS, R1, and PBL, indicating a 10-K-colder initial temperature

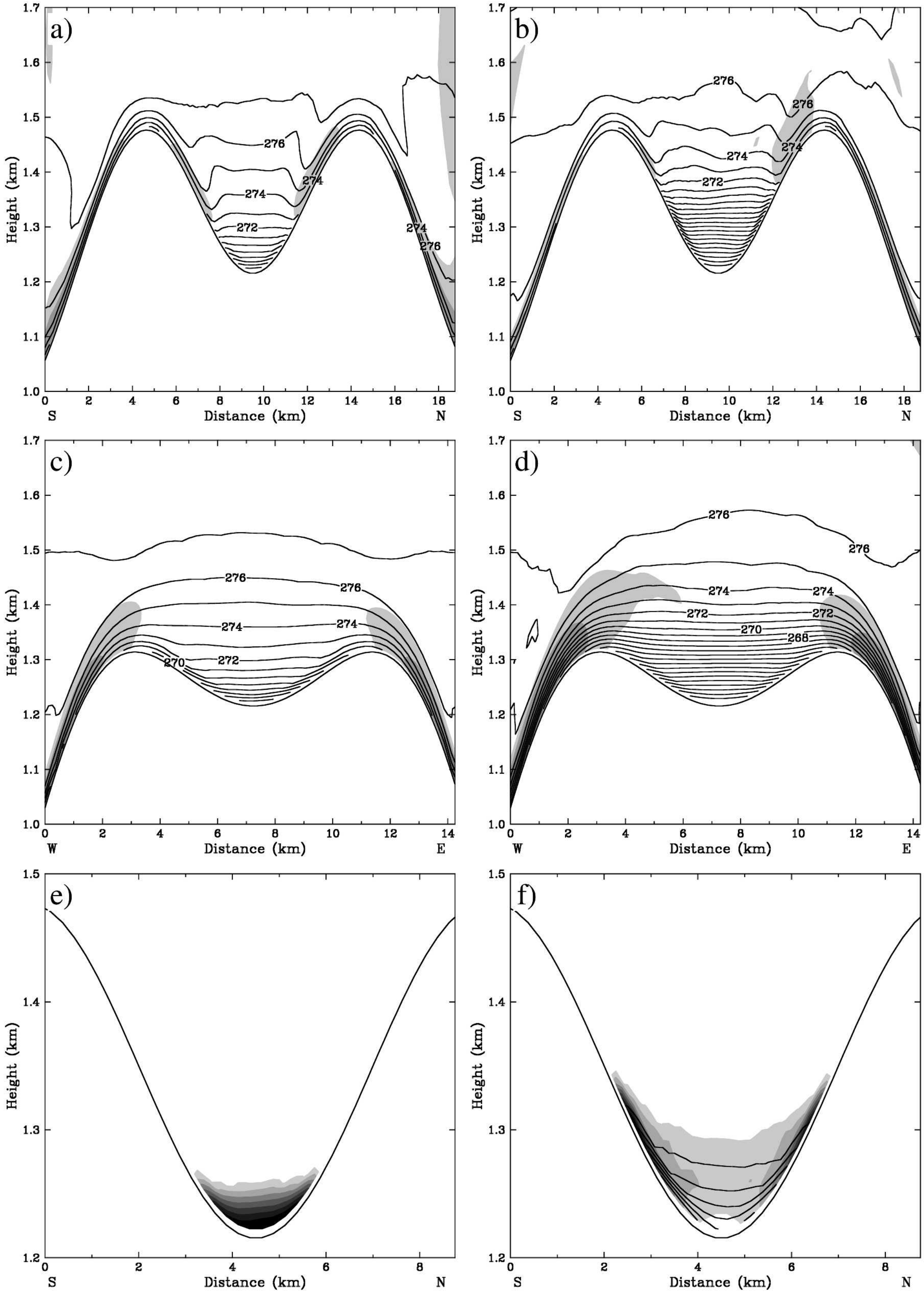

Fig. 4. (top) Vertical cross sections of potential temperature (contour interval 1 K) and wind speed (shading increment 2 m s^{-1}) along line a1–a2 (see Fig. 1b) at (a) 1600 and (b) 0800 LT. (middle) Same as (a) and (b), but following the line b1–b2 in Fig. 1b. Results are valid at (c) 1600 and (d) 0800 LT. (bottom) Cloud water mixing ratio (shading increment 0.02 g kg^{-1}) and cloud ice mixing ratio (contour interval 0.0025 g kg^{-1}) for the central part of line a1–a2: (e) 1600 and (f) 0800 LT.

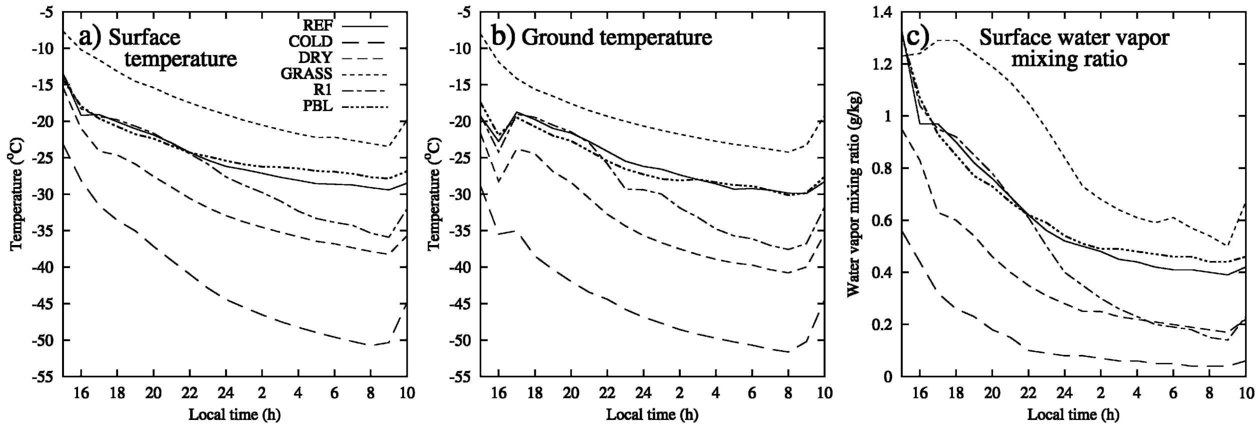

FIG. 5. Model output time series for (a) surface temperature, (b) ground temperature, and (c) surface water vapor mixing ratio. Results are valid for the grid point in the center of the sinkhole. The key given in (a) is valid for (b) and (c).

profile, a halved initial relative humidity, surface parameters for grassland in the sinkhole area, the Reisner1 microphysics scheme, and a closer-to-original version of the PBL scheme, respectively (see Table 1 for a summary). For all five experiments, time series of surface and ground temperature as well as surface mixing ratio are included in Fig. 5. For the COLD and GRASS experiments, Fig. 6 displays the surface temperature and mixing ratio fields at 0800 LT, and the corresponding vertical cross sections of potential temperature, wind speed, and cloud water/ice are shown in Fig. 7.

The results of the COLD run show that reducing the initial temperature by 10 K while retaining the initial relative humidity has a pronounced impact on the evolution of the cold-air pool. Compared to the REF run, the minimum temperature reached before sunrise is about 22 K lower, implying that the net cooling increases by 12 K because of the reduction of the initial

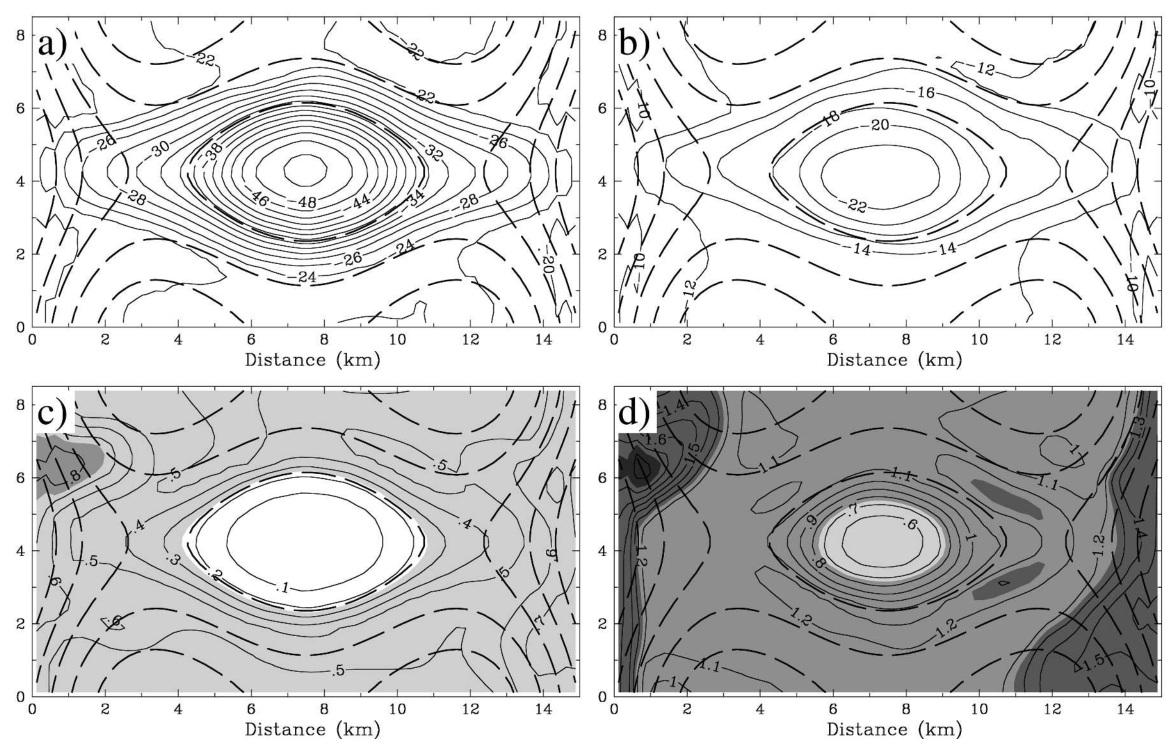

FIG. 6. (top) Surface temperature (contour interval 2°C) at 0800 LT for simulations (a) COLD and (b) GRASS. (bottom) Surface water vapor mixing ratio (contour interval 0.1 g kg^{-1}; shading starts at 0.25 g kg^{-1} with an increment of 0.5 g kg^{-1}) at 0800 LT for simulations (c) COLD and (d) GRASS.

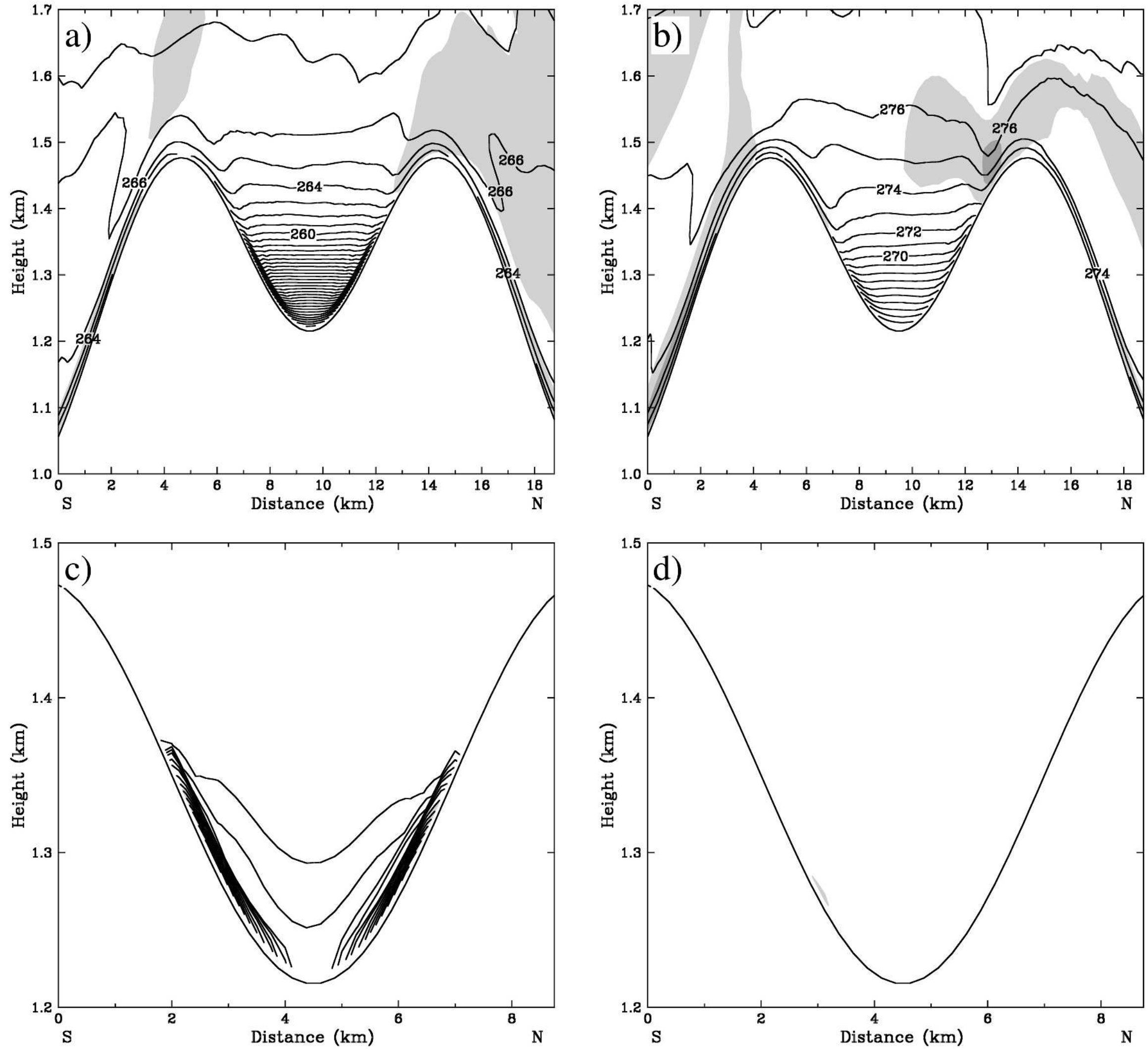

FIG. 7. (top) Same as Fig. 4b, but for simulations (a) COLD and (b) GRASS. (bottom) Same as Fig. 4f, but for simulations (c) COLD and (d) GRASS.

temperature. The surface temperature difference between the sinkhole center and outside now reaches 28 K (Fig. 6a), and the katabatic winds within the basin are even weaker than in REF because of the extreme static stability (Fig. 7a). It is also interesting to note that the ground temperature remains always colder than the air temperature in the COLD run and that the jump in the ground temperature after 1600 LT is much weaker than in REF (Figs. 5a,b). This indicates that the amount of cloud substance within the basin is much smaller in the COLD run than in the REF run, leading to a larger net radiative heat loss. In fact, there are no significant amounts of cloud water in the center region of the basin, and the cloud ice mixing ratio also remains below 0.0075 g kg^{-1} above the basin center (Fig. 7c). Larger amounts of cloud substance are again found along the side slopes (up to 0.025 g kg^{-1} of cloud ice and 0.03 g kg^{-1} of cloud water), but this is also much less than for the REF case. A discussion of the corresponding radiative heat fluxes will be given in the next section.

Further interesting results appear in the surface field of water vapor mixing ratio (Figs. 5c and 6c). Along with the extraordinarily strong cooling, the mixing ratio in the sinkhole center drops to 0.04 g kg^{-1} in the COLD run, which is an order of magnitude less than in the REF run. This implies impressive differences in the fractional drying of the near-surface air. While the mixing ratio decreases by a factor of 3.5 in the REF run, it decreases by a factor of 14 in the COLD run. Evidently, the dominance of ice clouds in the COLD run provides a much more effective drying than the mixture of water and ice clouds in the REF run. The drying process in the COLD run is also more effective than in the DRY run. Starting with only 10% more water vapor than the COLD run, the near-surface air gets moistened through evaporation from the ground during the first three hours of simulation in the DRY run. At the beginning of the drying phase (1500 LT), the surface mixing ratio in the sinkhole center therefore is about 60% larger in the DRY run than in the COLD run (Fig. 5c). Afterward, a drying by a factor of 6 is achieved in the DRY run, which is between the values for REF and COLD but closer to REF. The resulting minimum mixing ratio is about half as large as in the REF experiment (Fig. 5c), implying that the net drying is quite similar for REF and DRY. Note also that the total cooling obtained in the DRY run is still 4 K smaller than in the COLD run although the initial relative humidity is only half as large.

The importance of the surface texture is highlighted by the GRASS run, assuming a surface albedo and a surface heat capacity representative for grassland rather than powder snow. The main effect of the lower albedo is that the surface temperature at 1500 LT hardly differs from the initial (1200 LT) value. A shallow convectively mixed layer even forms during the first 2 h of simulation (not shown). After sunset, the larger surface heat capacity renders the cooling more gradual than for the cases with snow cover. The total cooling between initialization and sunrise is about 6 K smaller than for REF (Fig. 5a), and the temperature difference between the basin center and outside is only about 12 K at 0800 LT (Fig. 6b). Correspondingly, the static stability within the basin is substantially smaller than in the other cases (Fig. 7b). The comparatively gradual cooling occurring in the GRASS run also has the effect that no clouds form in the center region of the sinkhole. This is indirectly evident from Fig. 5b, giving no indication of a discontinuity in the ground cooling, and directly evident from Fig. 7d. A small amount of cloud water is found along the southern slope of the basin (Fig. 7d), and significant amounts of cloud water are restricted to the eastern and western side slopes (see Fig. 10c below). The mixing ratio fields (Figs. 5c and 6d) indicate that evaporation from the ground continues until 1700 LT. After 1800 LT, the near-surface air dries by a factor of more than 2, which is solely due to deposition of water vapor at the ground in this case.

The remaining experiments, R1 and PBL, investigate model-related sensitivities. For the fields displayed in Fig. 5, the PBL and REF runs hardly differ from each other, suggesting no need for a further discussion. However, the analysis of the heat and moisture budgets conducted in the next section will reveal some important differences, and a comparison with observations will show that the results of the PBL run are less realistic than those of the REF run. Comparing the REF and R1 experiments shows that R1 becomes significantly colder and drier after midnight, while the differences are small before. A closer analysis of the results revealed that these differences are mainly due to a different treatment of cloud ice. As soon as the temperature falls below $-25°C$, the Reisner1 scheme rapidly converts all cloud water into cloud ice that then falls to the ground. Given the fact that the threshold for homogeneous freezing of cloud droplets is near $-40°C$ (Pruppacher and Klett 1997), the smoother transition applied in the Reisner2 scheme appears to be more realistic. The Reisner1 scheme also tends to convert cloud ice more rapidly into snow than the Reisner2 scheme, which reinforces the excessive drying tendency of the Reisner1 scheme.

Before turning to the analysis of the heat and moisture budgets, the model results will be compared to the available observations. The most detailed observations (Clements et al. 2003) have been collected on days without snow cover, implying that they have to be compared with the GRASS experiment. Generally, the shape of the simulated surface temperature curves (rapid cooling in the early evening, more gradual cooling later on) is in good agreement with observed curves for undisturbed days (see also Sauberer and Dirmhirn 1956; Clements et al. 2003; Pospichal et al. 2003; Whiteman et al. 2004a,b). Moreover, the total cooling at the sinkhole bottom (17 K in the GRASS run) and the morning temperature difference between the sinkhole bottom and outside (12 K in the GRASS run) are within the observed range for undisturbed days without snow cover. Clements et al. (2003) also stress the extreme weakness of the katabatic flow down the slopes of the sinkhole and the presence of virtually calm conditions at the bottom of the sinkhole. On the other hand, significant cold-air outflow is observed at the lowest pass connecting the Gstettneralm sinkhole with the environment (Pospichal et al. 2003). Frequent observations of ground fog in the Gstettneralm sinkhole in the warm season (Sauberer and Dirmhirn 1954, 1956) confirm the importance of the above-mentioned drying processes, which require temperatures well below freezing to become effective. The most notable difference between the model results and the observations concerns the vertical temperature profile in the sinkhole, which tends to be smoother in the model than in reality. This is illustrated in Fig. 8, showing a comparison of the simulated potential temperature profile (GRASS run) at 0800 LT with tethersonde observations from the Gstettneralm sinkhole (note that the height axis is rescaled for the simulation so as to allow for a direct comparison with the observations; see figure caption). While the observed static stability tends to exhibit a pronounced local maximum near the level of the lowest connection with the environment (see also Sauberer and Dirmhirn 1954), the simulated temperature increase with height is more uniform. This deficiency is most likely related to the terrain-following coordinate used in the MM5, which is known to have problems with representing thin elevated inversions over sloping topography. Moreover, the limited vertical resolution of the simulations might play a role.

The characteristics of the simulations with a snow-covered sinkhole compare similarly well with the available observations. In particular, the dependence of the

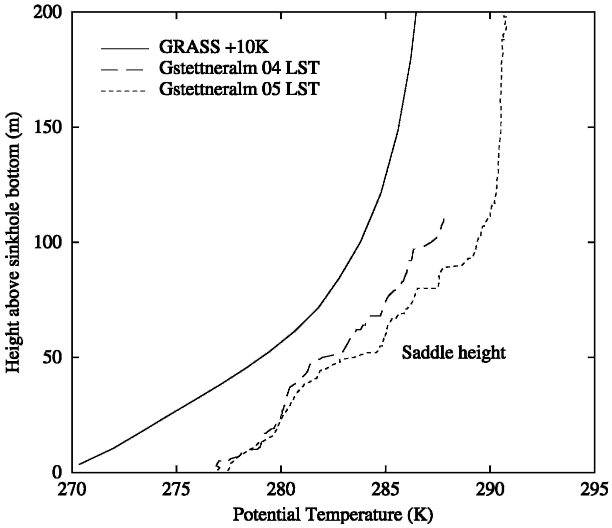

FIG. 8. Comparison of the simulated potential temperature profile of the GRASS run at 0800 LT with tethersonde observations from the Gstettneralm sinkhole (tethersonde data are courtesy of D. Whiteman). Observations were taken on 3 Jun 2002 at 0402 and 0514 LST. Note that the height axis is squeezed by a factor of 2 for the simulated profile in order to account for the differences in sinkhole depth (the height of the lowest saddle is 50 m for the Gstettneralm and 100 m for the model topography). Moreover, the simulated profile is shifted to the right by 10 K.

cooling rate and the basin-environment temperature difference on the ambient temperature is also evident in the observations made in the Gstettneralm sinkhole (Sauberer and Dirmhirn 1954, 1956; Whiteman et al. 2004b). On very cold days (temperature below −15°C outside the basin), observed temperature differences can exceed 25 K (e.g., Aigner 1952), but differences around 20 K are more frequent. In this context, it is important to note that the altitude of the model sinkhole is very close to that of the Gstettneralm sinkhole, so that the depth of the overlying atmosphere is virtually the same. Thus, the simulated radiative fluxes for a given temperature and moisture profile are representative for the Gstettneralm. Moreover, the ambient 850-hPa temperature of the COLD run (about −19°C) is representative for the conditions after an outbreak of continental polar air toward the Alps. Thus, the close agreement of the simulated surface temperature minimum in the cold run (−51°C) with the temperature minima reported by Aigner (1952) can be taken as a further indication of the realism of the simulations. No observational evidence seems to be available for ice crystal sedimentation in sinkholes, but this is not surprising since field campaigns have never been conducted in extremely cold winter nights (the available temperature data stem from data loggers). However, ice crystal sedimentation is a very common feature in polar regions (e.g., Bromwich 1988), so that it is reasonable to assume that it can occur in sinkholes as well. Indirect observations based on the structure of the snow surface might help to verify this model result.

4. Analysis of the heat and moisture budgets

The purpose of this section is to provide a deeper insight into the heat and moisture fluxes involved in the cooling process of the basin air. Time series for a number of quantities are displayed in Fig. 9. As for the time series shown in Fig. 5, they are evaluated at the model grid point lying in the center of the sinkhole. Figure 9a shows the downward longwave radiation, which is the only radiative heat source term between 1600 and 0800 LT. For the REF, COLD, GRASS, and R1 experiments, two-dimensional fields of the downward longwave radiation at 0800 LT are added in Fig. 10, providing an indirect measure of the cloud distribution in the basin. The four subsequent time series (Figs. 9b–e) constitute the heat budget terms of the first soil layer, representing the uppermost centimeter of the soil (or snow cover). The change in the local heat storage of this layer, which is not shown in Fig. 9, can be computed from the ground temperature evolution displayed in Fig. 5b. In units of Watts per meter squared, it is given by $3 \times 10^3 \dot{T}$ for snow and by $1.5 \times 10^4 \dot{T}$ for grass, with $\dot{T}$ denoting the temporal tendency of the ground temperature. This implies that a cooling of 1 K h^{-1} corresponds to a heat flux divergence of 0.83 and 4.16 W m^{-2} for snow and grass, respectively. Information on the evolution of the moisture field is provided in Figs. 9f–i. The integrated fields shown in Figs. 9f and 9i extend over the 10 lower model layers, corresponding to a layer depth of about 175 m. This depth has been chosen because it roughly represents the layer of significant nocturnal cooling over the basin center. Finally, surface fields of the sensible heat flux and the relative humidity are shown in Figs. 11 and 12, respectively.

The time series for the downward longwave radiation (Fig. 9a) indicate the formation of clouds above the basin center immediately after sunset for all experiments but GRASS. This is confirmed by the column-integrated total cloud water (i.e., water + ice) displayed in Fig. 9i. As a result of the cloud formation, the longwave radiation increases by about 15 W m^{-2} in the COLD run and by about 60 W m^{-2} in the other runs (except GRASS). The subsequent evolution strongly differs between the various experiments. The REF run exhibits a gradual decrease of the downward radiation, corresponding to the depletion of the cloud water by sedimenting cloud ice. However, the longwave radiation remains higher than it was before sunset. Initially, the R1 run (Reisner1 microphysics) almost coincides with the REF run, but the curves diverge after 2200 LT when the temperature in the sinkhole center falls below −25°C. As mentioned above, the Reisner1 scheme converts all the cloud water into cloud ice below this temperature, leading to an unrealistically rapid drying of the basin atmosphere (see also Figs. 9g and 9i). This threshold dependence also becomes evident from comparing Figs. 10a and 10d. In the outer part of the basin, the cloud density (and therefore the downward long-

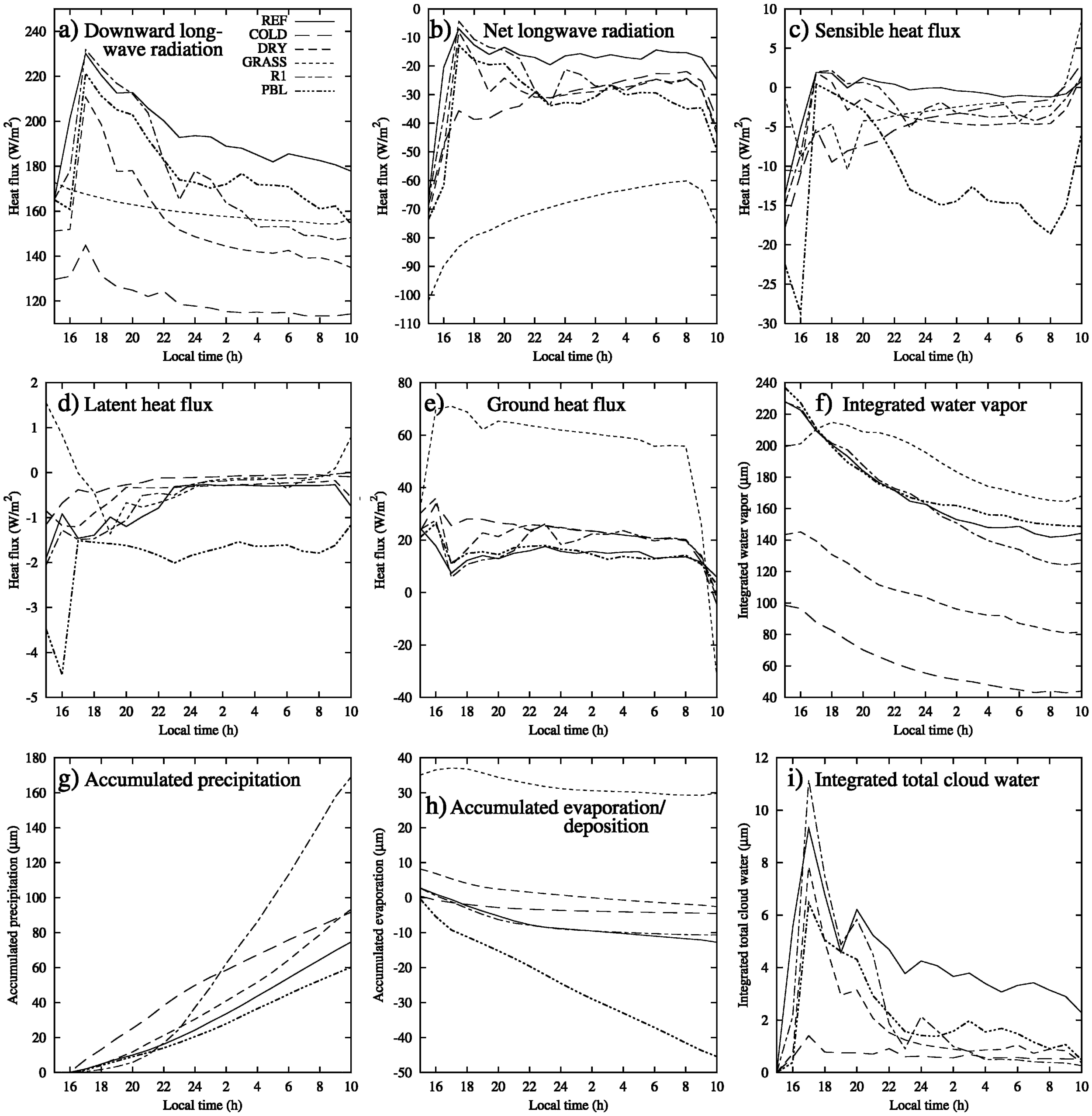

FIG. 9. Model output time series for (a) downward longwave radiation, (b) net longwave radiation, (c) sensible heat flux, (d) latent heat flux, (e) ground heat flux, (f) integrated water vapor, (g) accumulated precipitation, (h) accumulated evaporation/deposition, and (i) integrated total cloud water. Results are valid for the grid point in the center of the sinkhole. The integrated quantities refer to the lower 10 model levels, representing a layer depth of about 175 m. The key given in (a) is valid for all panels.

wave radiation) is quite similar in both experiments, but in the center region, a pronounced window opens in R1 while the cloud deck remains closed in REF. Next, the PBL run exhibits less downward longwave radiation than the REF run throughout the time, but the shape of the curves is quite similar. This difference is mainly because the deposition of water vapor at the ground is larger in PBL than in REF (Fig. 9h). The DRY run exhibits a more rapid and effective depletion of the cloud water than the REF run despite the same physics parameterizations because of its lower temperature level. This is even more so for the COLD run, in which cloud ice dominates over cloud water from the start (see also Fig. 9g). Finally, the GRASS run exhibits a gradual decrease of the longwave radiation throughout the night, which is related to the steady cooling and drying of the air within the basin. The presence of a positive feedback effect of the cold pool on the down-

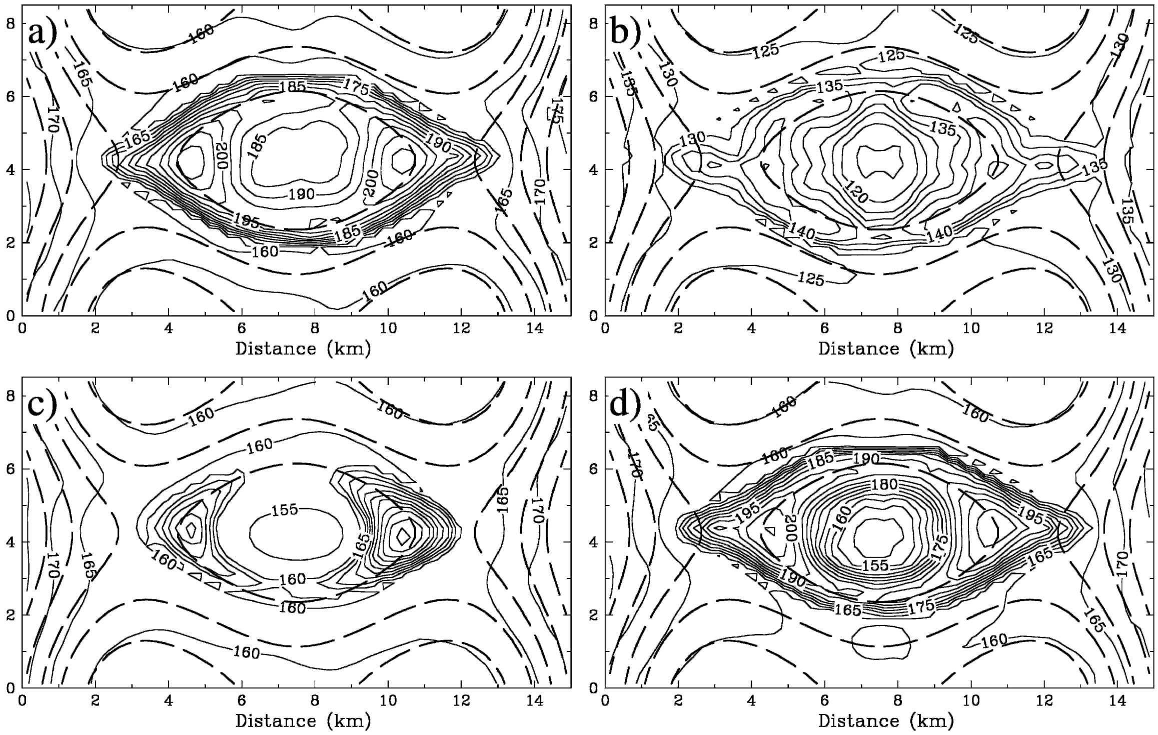

FIG. 10. Downward longwave radiation (contour interval 5 W m^{-2}) at 0800 LT for simulations (a) REF, (b) COLD, (c) GRASS, and (d) R1.

ward longwave radiation is confirmed by Figs. 10b–d. The COLD, GRASS, and R1 runs all have less downward radiation in the basin center than outside the basin, even though there is a small amount of cloud substance present in COLD and R1.

The most important terms of the ground heat budget are the net longwave radiation (Fig. 9b), which also accounts for the surface emissivity, and the ground heat flux (Fig. 9e). The sensible heat flux (Figs. 9c and 11) is small except for the PBL run, and the latent heat flux (Fig. 9d) is of minor importance in all simulations. Correspondingly, the ground heat flux is the leading term opposing the net radiation in all cases but PBL. The degree of cancellation is largest in the GRASS case, where a net radiative heat loss of more than 60 W m^{-2} is opposed by a ground heat flux that is only a few Watts per meter squared smaller. This is, as already mentioned, the reason for the comparatively high sinkhole temperatures in the GRASS run. In the simulations with snow cover, the nocturnal radiative heat loss ranges between 10 and 40 W m^{-2}, depending on the amount of clouds present above the sinkhole center. Note that the differences among the various simulations (except GRASS) are much smaller for the net

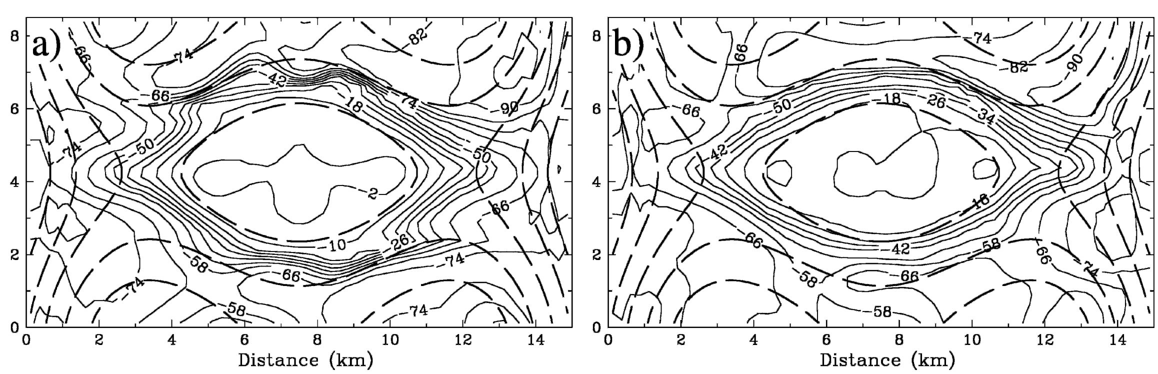

FIG. 11. Surface sensible heat flux (contour interval 8 W m^{-2}; highest contour at -2 W m^{-2}) at 0800 LT for simulations (a) REF and (b) PBL.

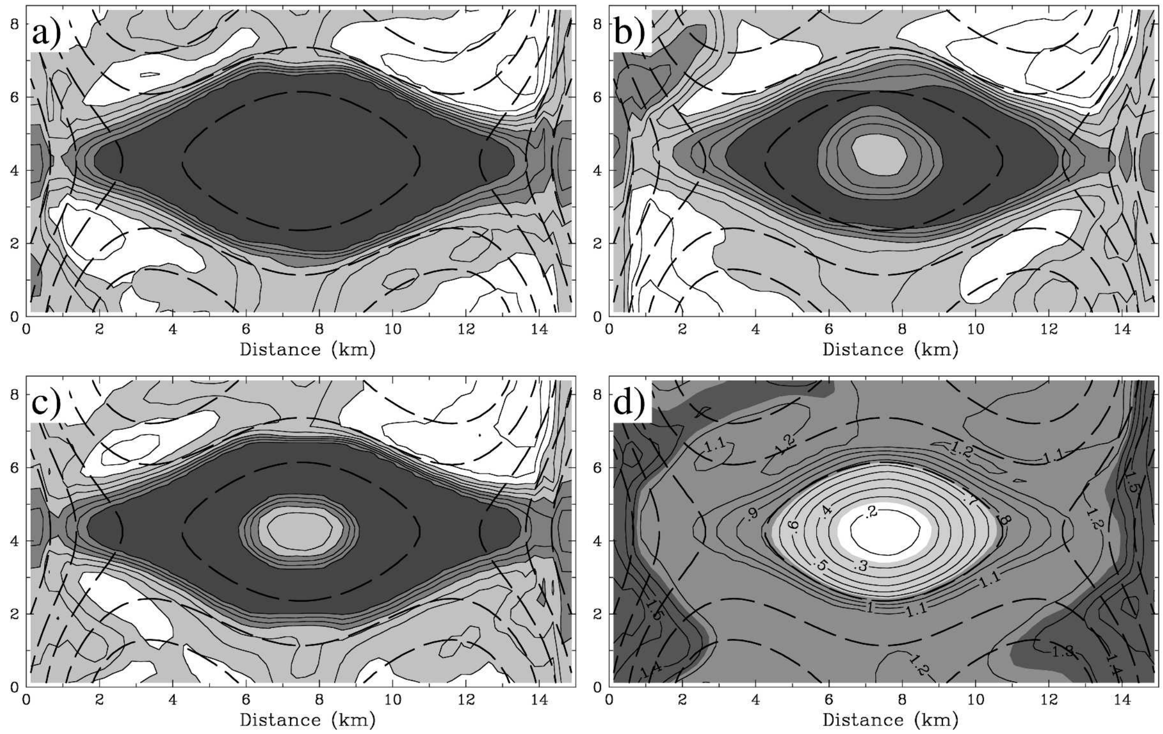

FIG. 12. (a)–(c) Surface relative humidity (contour interval 5%; shading starts at 65% with an increment of 15%) at 0800 LT for simulations (a) REF, (b) GRASS, and (c) R1. (d) Surface water vapor mixing ratio at 0800 LT for simulation R1; plotting conventions are as in Fig. 6c.

radiation than for the total downward radiation, indicating that an important fraction of the radiation differences is directly converted into differences of the ground temperature. A comparison with observations of the heat budget terms (Sauberer and Dirmhirn 1956; Clements et al. 2003) indicates that the net radiative heat loss obtained from the GRASS run, including its temporal evolution, is very realistic. Since the cooling rates of the near-surface air are also in agreement with observations, there is indirect evidence that the simulated ground heat fluxes are realistic, too. For situations with snow cover, quantitative measurements of the radiation budgets are not yet available, but Sauberer and Dirmhirn (1954) report that the radiation balance remains significantly negative throughout the night. Moreover, Clements et al. (2003) found that the sensible heat fluxes at the sinkhole bottom are close to zero during most of the night. This provides clear evidence that the vertical heat fluxes computed in the PBL run are unrealistically large and led to the decision to use the modified version of the Gayno–Seaman PBL scheme (strongly reduced lower threshold values for the TKE and the friction velocity) as standard. Note that the sensible heat fluxes outside the cold-air pool show only random differences between REF and PBL (Fig. 11), indicating that the thresholds set in the original version of the PBL scheme do not play a role in this region. However, the sensible heat fluxes differ by an order of magnitude in the central part of the sinkhole.

Finally, the water budget of the air in the sinkhole remains to be discussed. As already mentioned above, the integrated water vapor and total cloud water (water + ice) time series displayed in Figs. 9f and 9i represent a 175-m-deep layer above the ground. This is sufficient to enclose the air mass affected by the freeze-drying for all simulations. The accumulated precipitation and evaporation are shown in Figs. 9g and 9h, respectively. The units used to display these quantities are microns water equivalent in all cases, and a negative slope in the accumulated evaporation means that deposition of water vapor occurs at the ground.

For the reference run, the water budget shows that the water vapor column decreases by about 85 μm between 1500 LT and sunrise. Most of this is accomplished by precipitation (almost 75 μm), and deposition contributes slightly less than 15 μm. The approximate balance between the water vapor loss and the sum of the sink terms indicates that advective and diffusive moisture fluxes do not make a significant contribution in the REF case. The storage term (integrated total cloud water) is about 3 μm at sunrise and therefore also small. For the other simulations, the balance between the water vapor loss and the sink terms is not as good. For the PBL run, the total water vapor loss is similarly large as in REF, but the sum of the precipitation and deposition terms yields about 105 μm because of the (probably unrealistically) large deposition. A closer analysis revealed that this imbalance is mainly due to the vertical diffusion, leading to a downward moisture flux through the top of the considered column. The imbalance is even larger for the R1 run, where a water vapor loss of 105 μm contrasts with sink terms of 180 μm. In this case, the dominant transport toward the central column is by horizontal diffusion, reflecting the large horizontal moisture gradient within the basin (cf. Figs. 3b and 12d). The large moisture gradient in turn is a consequence of the unrealistic cloud ice generation of the Reisner1 scheme (see discussion above), leading to a kink in the precipitation rate when the temperature drops below $-25°$C. A substantial imbalance is also found for the DRY and COLD runs, in which the sum of the sink terms exceeds the integrated water vapor loss by about 50%. In these experiments, the freeze-drying induced by cloud ice formation reaches higher up than the lowest connection of the sinkhole to the environment, implying that the layer of positive vertical mixing ratio gradients reaches out of the closed part of the basin. There, subsiding motion prevails and leads to a moistening of the air column by vertical advection. Supporting evidence for this explanation can be found by considering the temporal evolution of the water vapor column and the sink terms. The terms are in close balance up to midnight (COLD) and 0400 LT (DRY), reflecting the time period in which the cloud ice is restricted to the closed part of the basin. Later on, as the cloud ice starts to extend higher up, the curves progressively diverge.

A separate discussion is required for the GRASS run, which exhibits a substantially larger water vapor loss than provided by the sink terms shown in Figs. 9g and 9h (no precipitation in GRASS). Moreover, the integrated water vapor at 1500 LT is significantly smaller than in REF, although the accumulated evaporation (Fig. 9h) reaches quite a high level during the first 3 h of simulation. The latter feature can be explained by the fact that a 500-m-deep convectively mixed layer is established in the early afternoon, leading to a mixing of the basin air with drier air originally located at higher levels. Later on, subsidence in the upper part of the basin again leads to a drying of the air. A separate calculation conducted for a 75-m-deep column (not shown) revealed that the deposition of water vapor at the ground (Fig. 9h) accounts for the drying of the near-surface air, while the remaining drying can be ascribed to advective effects.

It is interesting to note that the depositional drying in the GRASS run is able to keep the relative humidity at the lowermost model level close to ice saturation, corresponding to a relative humidity (which is defined with respect to water) of slightly below 80% in the center of the sinkhole (Fig. 12b). In the REF run, however, the deposition process is too slow to keep the near-surface humidity below water saturation (Fig. 12a). Near-surface humidities below water saturation are also found in R1 (Fig. 12c), which is related to the excessive cloud ice formation occurring in the Reisner1 scheme, and in the PBL and COLD experiments (not shown). In the PBL run, the subsaturation is mainly related to the stronger deposition (Fig. 9h), while in the COLD experiment, the homogeneous ice nucleation active at temperatures below $-40°$C provides a sufficiently effective drying of the air.

5. Discussion and conclusions

Idealized numerical simulations have been conducted to investigate the formation of extreme cold-air pools in elevated sinkholes. The simulations have been performed with MM5, which has been modified in several aspects to obtain sufficient accuracy for the problem under scrutiny. The most important modifications affect the calculation of horizontal diffusion, which can induce large systematic errors in the original MM5 (Zängl 2002), and the boundary layer parameterization, from which several lower threshold values related to vertical mixing had to be removed. A comparison with observed sensible heat fluxes revealed that retaining the original threshold values would lead to unrealistically large heat fluxes within the cold-air pool. However, a good agreement with the available observations is obtained with the modified model version.

According to the model results, the most important requirements for the formation of extreme cold-air pools in sinkholes are a small heat conductivity of the ground and a mechanism extracting moisture from the basin air during the cooling process. While the impact of the first factor has already been inferred from the fact that extremely low temperature minima are always connected to the presence of freshly fallen snow, the drying process has received very little attention so far. Its crucial importance lies in the fact that a temperature decrease from $-20°$ to $-50°$C, as observed in extreme cases, is associated with a reduction of the saturation water vapor pressure by a factor of 20. Unless the initial relative humidity is exceptionally low, the nocturnal cooling of the air in a sinkhole must therefore be accompanied by substantial drying in order to prevent the formation of fog, which in turn would dramatically decrease the radiative heat loss. Near the surface, such drying can be accomplished by water vapor deposition at the ground. This process can become quite effective at low temperatures because the vapor pressure over ice is substantially lower than over water (e.g., by a factor of 1.33 at $-30°$C). However, despite considerable uncertainty related to the cloud microphysics parameterization, the model results suggest that the formation of cloud ice particles is even more important when considering the basin as a whole. Unlike water droplets, ice particles have a significant sedimentation speed ($\sim$25 cm s^{-1}), enabling them to effectively remove moisture from the atmosphere. Because of the above-mentioned differences in the vapor pressure, cloud ice particles are even able to grow at the expense of surrounding water droplets, thereby partly dissolving previously formed water clouds. Most of the uncertainty in modeling cloud ice formation in sinkholes is due to the fact that at temperatures above $-40°C$, an appropriate aerosol particle is needed to allow a cloud droplet to turn into an ice particle (Pruppacher and Klett 1997). The assumptions made in existing cloud models on the abundance of these so-called ice-forming nuclei might not be valid for mountain sinkholes (but there is no way to check this because of a complete lack of data), so that the related drying efficiency might also be wrong. A better reliability can be expected at temperatures below $-40°C$ because cloud ice formation is then possible through homogeneous freezing (i.e., without the presence of an ice-forming nucleus).

Further noteworthy results that can be inferred from our simulations concern the influence of the sinkhole depth. As already pointed out by Geiger (1965), the fact that a cold-air pool of finite depth reduces the downward longwave radiation suggests a positive feedback between the cold-pool depth and the temperature difference between the sinkhole bottom and the environment. The present model results support the presence of such a positive feedback, showing that the longwave radiation in the center region of the cold pool is up to 10 W m^{-2} lower than outside. However, it also has to be mentioned that Geiger (1965) overemphasized the importance of this effect. Based on a radiative flux calculation made for the standard atmosphere, he asserted that 72% of the longwave counterradiation originate from the lowest 87 m of the atmosphere, giving way to a tremendous feedback effect when the cold-pool depth is of the order of 100 m. The problem with this calculation is that the infrared optical thickness of the atmosphere depends strongly on its moisture content, which is two orders of magnitude lower at a temperature of $-40°C$ than at a temperature of $+15°C$. In fact, measurements in secondary sinkholes in the Gstettneralm region presented by Whiteman et al. (2004b) indicate that a factor of 2 difference in the depth of a sinkhole (25 versus 50 m) has only a minor impact ($\sim$1 K) on the surface temperatures. This also implies that the comparatively large depth of our idealized sinkhole, which was mainly motivated by numerical considerations, should not degrade the comparability of the present model results with observations in the Gstettneralm or Peter Sinks basins. A systematic dependence on the sinkhole depth is expected only for the importance of ice crystal sedimentation because the integrated amount of drying required to keep the air below saturation decreases with the sinkhole depth. The drying accomplished by vapor deposition at the ground, which should be largely independent from the sinkhole depth, might already be sufficient to prevent fog formation in very shallow sinkholes.

Further refinements of the present modeling approach will be needed for studying the temperature evolution in smaller sinkholes with significantly steeper sidewalls. Such sinkholes tend to stay warmer than shallow sinkholes because the reduced sky-view factor increases the downward longwave radiation (Whiteman et al. 2004b). Accounting for these effects requires a fully three-dimensional radiative transfer scheme, which is presently not available in the MM5. Simulating the breakup of a cold pool in a sinkhole may also require a more sophisticated treatment of radiation, because reflection of solar radiation into the shaded part of the basin could have a nonnegligible impact on the energy balance. Moreover, inhomogeneities in the surface albedo (e.g., because of trees in a snow-covered environment) certainly affect the evolution of cold-pool breakup.

Acknowledgments. I would like to express my gratitude to Dave Whiteman for providing the data shown in Fig. 8 and for his instructive comments on an earlier version of this paper. The comments made by the anonymous reviewers are also acknowledged.

REFERENCES

Aigner, S., 1952: Die Temperaturminima im Gstettnerboden bei Lunz am See, Niederösterreich (The temperature minima at the Gstettnerboden near Lunz am See, lower Austria). *Wetter Leben,* **5,** 34–37.

Bader, D. C., and T. B. McKee, 1983: Dynamical model simulation of the morning boundary layer development in deep mountain valleys. *J. Climate Appl. Meteor.,* **22,** 341–351.

Bromwich, D. H., 1988: Snowfall in high southern latitudes. *Rev. Geophys.,* **26,** 149–168.

Clements, C. B., C. D. Whiteman, and J. D. Horel, 2003: Cold-air-pool structure and evolution in a mountain basin: Peter Sinks, Utah. *J. Appl. Meteor.,* **42,** 752–768.

Colette, A., F. K. Chow, and R. L. Street, 2003: A numerical study of inversion-layer breakup and the effects of topographic shading in idealized valleys. *J. Appl. Meteor.,* **42,** 1255–1272.

Garnier, B. J., and A. Ohmura, 1968: A method of calculating the direct shortwave radiation income of slopes. *J. Appl. Meteor.,* **7,** 796–800.

Geiger, R., 1965: *The Climate near the Ground.* Harvard University Press, 611 pp.

Grell, G. A., J. Dudhia, and D. R. Stauffer, 1995: A description of the fifth-generation Penn State/NCAR Mesoscale Model (MM5). NCAR Tech. Note NCAR/TN-398+STR, 122 pp.

Mlawer, E. J., S. J. Taubman, P. D. Brown, M. J. Iacono, and S. A. Clough, 1997: Radiative transfer for inhomogeneous atmosphere: RRTM, a validated correlated-k model for the longwave. *J. Geophys. Res.,* **102,** 16 663–16 682.

Petkovšek, Z., 1985: Die Beendigung von Luftverunreinigungsperioden in Talbecken (The termination of air pollution periods in basins). *Z. Meteor.,* **35,** 370–372.

——, 1992: Turbulent dissipation of cold air lake in a basin. *Meteor. Atmos. Phys.,* **47,** 237–245.

——, and T. Vrhovec, 1994: Note on influences of inclined fog lakes on the air pollution in them and on the irradiance above them. *Meteor. Z.,* **3,** 227–232.

Pospichal, B., S. Eisenbach, C. D. Whiteman, R. Steinacker, and M. Dorninger, 2003: Observations of the cold air outflow from a basin cold pool through a low pass. *Proc. Int. Conf. on Alpine Meteorology and MAP Meeting 2003,* Vol. 66, Brig, Switzerland, MeteoSwiss, 153–156.

Pruppacher, H. R., and J. D. Klett, 1997: *Microphysics of Clouds and Precipitation.* Kluwer Academic, 954 pp.

Rakovec, J., J. Merše, S. Jernej, and B. Paradiž, 2002: Turbulent disspation of the cold-air pool in a basin: Comparison of observed and simulated development. *Meteor. Atmos. Phys.,* **79,** 195–213.

Reisner, J., R. M. Rasmussen, and R. T. Bruintjes, 1998: Explicit forecasting of supercooled liquid water in winter storms using the MM5 mesoscale model. *Quart. J. Roy. Meteor. Soc.,* **124,** 1071–1107.

Sauberer, F., and I. Dirmhirn, 1954: Über die Entstehung der extremen Temperaturminima in der Doline Gstettner-Alm (On the development of the extreme temperature minima in the Gstettner-Alm sinkhole). *Arch. Meteor. Geophys. Bioklimatol.,* **B5,** 307–326.

——, and ——, 1956: Weitere Untersuchungen über die Kaltluftansammlungen in der Doline Gstettner-Alm bei Lunz in Niederösterreich (Further investigations of the cold-air pools in the Gstettner-Alm sinkhole near Lunz in lower Austria). *Wetter Leben,* **8,** 187–196.

Schmidt, W., 1930: Die tiefsten Minimumtemperaturen in Mitteleuropa (Record temperature minima in central Europe). *Naturwissenschaften,* **18,** 367–369.

Shafran, P. C., N. L. Seaman, and G. A. Gayno, 2000: Evaluation of numerical predictions of boundary layer structure during the Lake Michigan Ozone Study (LMOS). *J. Appl. Meteor.,* **39,** 412–426.

Vrhovec, T., 1991: A cold air lake formation in a basin—A simulation with a mesoscale numerical model. *Meteor. Atmos. Phys.,* **8,** 91–99.

Whiteman, C. D., and T. B. McKee, 1982: Breakup of temperature inversions in deep mountain valleys: Part II. Thermodynamic model. *J. Appl. Meteor.,* **21,** 290–302.

——, S. Eisenbach, B. Pospichal, and R. Steinacker, 2004a: Comparison of vertical soundings and sidewall air temperature measurements in a small Alpine basin. *J. Appl. Meteor.,* **43,** 1635–1647.

——, T. Haiden, B. Pospichal, S. Eisenbach, and R. Steinacker, 2004b: Minimum temperatures, diurnal temperature ranges and temperature inversions in limestone sinkholes of different size and shape. *J. Appl. Meteor.,* **43,** 1224–1236.

Zängl, G., 2002: An improved method for computing horizontal diffusion in a sigma-coordinate model and its application to simulations over mountainous topography. *Mon. Wea. Rev.,* **130,** 1423–1432.

——, 2003a: The impact of upstream blocking, drainage flow and the geostrophic pressure gradient on the persistence of cold air pools. *Quart. J. Roy. Meteor. Soc.,* **129,** 117–137.

——, 2003b: A generalized sigma coordinate system for the MM5. *Mon. Wea. Rev.,* **131,** 2875–2884.

Zhong, S., C. D. Whiteman, X. Bian, W. J. Shaw, and J. M. Hubbe, 2001: Meteorological processes affecting the evolution of a wintertime cold air pool in the Columbia basin. *Mon. Wea. Rev.,* **129,** 2600–2613.

——, X. Bian, and C. D. Whiteman, 2003: Time-scale for cold-air pool breakup by turbulent erosion. *Meteor. Z.,* **12,** 229–233.